PHYSICAL REVIEW B **82**, 104117 (2010)

Epitaxial strain effects in the spinel ferrites $CoFe_2O_4$ and $NiFe_2O_4$ from first principles

Daniel Fritsch* and Claude Ederer

School of Physics, Trinity College Dublin, Dublin 2, Ireland

(Received 25 June 2010; revised manuscript received 30 August 2010; published 23 September 2010)

The inverse spinels $CoFe_2O_4$ and $NiFe_2O_4$, which have been of particular interest over the past few years as building blocks of artificial multiferroic heterostructures and as possible spin-filter materials, are investigated by means of density-functional theory calculations. We address the effect of epitaxial strain on the magnetocrystalline anisotropy and show that, in agreement with experimental observations, tensile strain favors perpendicular anisotropy whereas compressive strain favors in-plane orientation of the magnetization. Our calculated magnetostriction constants λ_{100} of about -220 ppm for $CoFe_2O_4$ and -45 ppm for $NiFe_2O_4$ agree well with available experimental data. We analyze the effect of different cation arrangements used to represent the inverse spinel structure and show that both local spin-density approximation plus U and generalized gradient approximation plus U allow for a good quantitative description of these materials. Our results open the way for further computational investigations of spinel ferrites.

DOI: 10.1103/PhysRevB.82.104117 PACS number(s): 75.80.+q, 75.70.Ak, 71.15.Mb, 75.47.Lx

I. INTRODUCTION

Spinel ferrites $CoFe_2O_4$ and $NiFe_2O_4$ are insulating magnetic oxides with high magnetic ordering temperatures and large saturation magnetizations.[1] This rare combination of properties makes them very attractive for a wide range of applications. Recently, particular attention has been focused on the possible use of spinel ferrites as magnetic components in artificial multiferroic heterostructures[2–5] or as spin-filtering tunnel barriers for spintronics devices.[6–8]

For these applications, the corresponding materials have to be prepared either in the form of thin films, grown on different substrates, or as components of more complex epitaxial heterostructures.[2,9–11] Due to the mismatch in lattice constants and thermal-expansion coefficients between the thin-film material and the substrate, significant amounts of strain can be incorporated in such epitaxial thin-film structures, depending on the specific growth conditions and substrate materials. This epitaxial strain can then lead to drastic changes in the properties of the thin-film material. Indeed, a reorientation of the magnetic easy axis under different conditions has been reported for $CoFe_2O_4$,[12–14] and a strong enhancement of magnetization and conductivity has been observed in $NiFe_2O_4$ thin films.[10,15,16]

In order to efficiently optimize the properties of thin-film materials, it is important to clarify whether the observed deviations from bulk behavior are indeed due to the epitaxial strain or whether they are induced by other factors, such as for example defects, off-stoichiometry, or genuine interface effects. First-principles calculations based on density-functional theory (DFT),[17–19] can provide valuable insights in this respect by allowing to address each of these effects separately.

Here we present results of DFT calculations for the structural and magnetic properties of epitaxially strained $CoFe_2O_4$ and $NiFe_2O_4$, with special emphasis on strain-induced changes in the magnetocrystalline anisotropy energy (MAE). Our results are representative for (001)-oriented thin films of $CoFe_2O_4$ and $NiFe_2O_4$, grown on different lattice-mismatched substrates. Our results provide important reference data for the interpretation of experimental observations in spinel ferrite thin films and in heterostructures consisting of combinations of spinel ferrites with other materials, such as perovskite structure oxides.

We find a large and strongly strain-dependent MAE for $CoFe_2O_4$, and a smaller but also strongly strain-dependent MAE for $NiFe_2O_4$. We discuss the influence of different cation arrangements within the inverse spinel structure and analyze the difference in the structural and magnetic properties due to different exchange-correlation functionals used in the calculations. From our calculations, we obtain the magnetostriction constants λ_{100} for both $CoFe_2O_4$ and $NiFe_2O_4$, which agree well with available experimental data.

This paper is organized as follows. Section II A gives a brief overview over the properties of $CoFe_2O_4$ and $NiFe_2O_4$ that are important for the present work and also summarizes results of previous DFT calculations. The basic equations governing the magnetoelastic properties of cubic crystals are presented in Sec. II B, followed by a detailed description of the structural relaxations performed in this work in Sec. II C, and a summary of further computational details in Sec. II D. The results of the bulk structural properties will be presented in Sec. III A whereas the effect of strain on the structural properties is analyzed in Sec. III B. The effect of strain on the MAE is discussed in Sec. III C. Finally, in Sec. IV a summary of our main conclusions is given.

II. BACKGROUND AND COMPUTATIONAL DETAILS

A. Spinel structure and previous work on ferrites

The spinel structure (space group $Fd\bar{3}m$, general formula AB_2X_4) contains two inequivalent cation sites, the tetrahedrally coordinated A site (T_d symmetry, Wyckoff position 8a), and the octahedrally coordinated B site (O_h symmetry, Wyckoff position 16d). In the *normal spinel* structure, all A sites are occupied by one cation species (divalent cation) whereas all B sites are occupied by the other cation species (trivalent cation). On the other hand, in the *inverse spinel* structure the trivalent cations occupy all A sites as well as

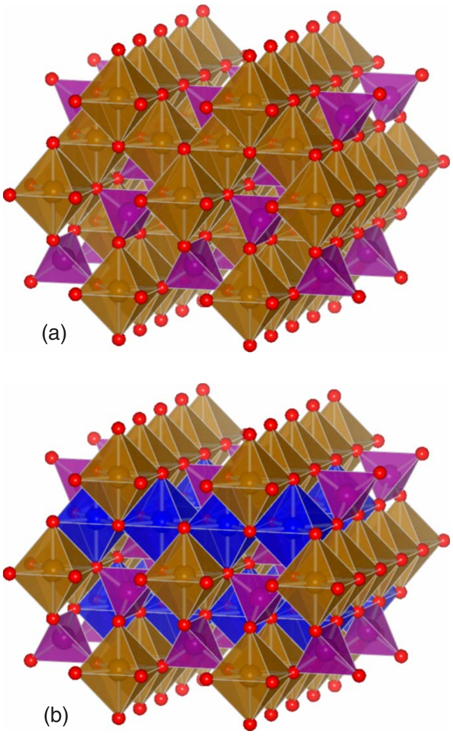

FIG. 1. (Color online) Inverse spinel structure of spinel ferrites. Oxygen cations are depicted as small red spheres (corner positions), and the coordination polyhedra surrounding cation sites are shaded. (a) Random cation distribution on the octahedrally coordinated *B* sites, i.e., all *B* sites remain equivalent. (b) *Imma* cation arrangement used throughout this work. Inequivalent *B* sites are represented by different shadings of the corresponding octahedra.

50% of the *B* sites whereas the remaining 50% of the *B* sites are occupied by the divalent cations. If the distribution of divalent and trivalent cations on the *B* sites is completely random, all *B* sites remain crystallographically equivalent and the overall cubic $Fd\bar{3}m$ symmetry is preserved [see Fig. 1(a)].

Both $CoFe_2O_4$ and $NiFe_2O_4$ crystallize in the inverse spinel structure, even though for $CoFe_2O_4$ the inversion is typically not fully complete, i.e., there is a nonzero Co^{2+} occupation on the *A* site. Thereby, the exact degree of inversion depends strongly on the preparation conditions.[1] To the best of our knowledge, no deviations from cubic symmetry have been reported for either system, i.e., the Co^{2+}/Ni^{2+} cations are believed to be randomly distributed on the *B* sites.[20]

According to the formal d^5 and d^7 electron configurations corresponding to Fe^{3+} and Co^{2+}, respectively, these ions can, in principle, exhibit both high-spin and low-spin states but only the high-spin states are experimentally observed in both spinel ferrites. For the d^8 electron configuration of Ni^{2+}, no such distinction exists. The magnetic moments of the *A*-site cations are oriented antiparallel to the magnetic moments of the *B*-site cations: the so-called Néel-type ferrimagnetic arrangement.[21] Thus, the magnetic moments of the Fe^{3+} cations on the *A* and *B* sites cancel each other exactly, and the net magnetization is mainly due to the divalent *B*-site cations, i.e., either Co^{2+} or Ni^{2+}. This results in a magnetic moment per formula unit close to the formal values of 3 μ_B and 2 μ_B in $CoFe_2O_4$ and $NiFe_2O_4$, respectively. Deviations from these values can be either due to orbital contributions to the magnetic moments or due to incomplete inversion and off-stoichiometric cation distribution.

Both $CoFe_2O_4$ and $NiFe_2O_4$ are small gap insulators but information on the experimental gap size is very limited. Waldron used infrared spectra to obtain threshold values of 0.11 and 0.33 eV for the electronic transitions in $CoFe_2O_4$ and $NiFe_2O_4$, respectively,[22] whereas Jonker estimated the energy gap in $CoFe_2O_4$ to be 0.55 eV, based on resistivity measurements along with other methods.[23]

Theoretical calculations of the electronic structure of spinel ferrites so far have been focused mostly on magnetite (Fe_3O_4). This material can be viewed as parent compound for the spinel ferrites, including $CoFe_2O_4$ and $NiFe_2O_4$, which are obtained by substituting the Fe^{2+} cation in magnetite by a different divalent 3*d* transition metal cation. In an early work, Pénicaud *et al.* performed DFT calculations within the local spin-density approximation (LSDA) for magnetite and the respective Co-, Ni-, Mn-, and Zn-substituted ferrites.[24] The use of LSDA leads to half-metallic band structures for all systems except $NiFe_2O_4$, in contrast to the insulating character observed experimentally. (We note that the case of magnetite is somewhat more involved than that of the other spinel ferrites since magnetite exhibits a metal-insulator transition at ~120 K.) It was later shown by Antonov *et al.* that insulating solutions for Co-, Ni-, and Mn-substituted Fe_3O_4 can be obtained within the LSDA+*U* approach.[25] The same was found by Szotek *et al.* using a self-interaction-corrected LSDA approach.[26] The latter study also addressed the energetic difference between normal and inverse spinel structures with different valence configurations. The electronic structure of $NiFe_2O_4$ was also calculated within a hybrid functional approach, where a large band gap of 4 eV was obtained by using 40% of Hartree-Fock exchange in the exchange-correlation energy functional.[27] Recently, Perron *et al.* investigated different magnetic arrangements for $NiFe_2O_4$ in both normal and inverse spinel structures using both LSDA and the generalized gradient approximation (GGA), and found the inverse spinel structure with Néel-type ferrimagnetic order to be energetically most favorable,[28] in agreement with the experimental observations.

Calculations of the MAE in strained $CoFe_2O_4$ and $NiFe_2O_4$ have been reported by Jeng and Guo.[29,30] However, due to the use of the LSDA, these calculations were based on half-metallic band structures for both materials. Furthermore, no information on structural properties or the influence of the specific cation arrangement used in the calculation was given.

B. Magnetoelastic energy of a cubic crystal

In this work, we are concerned with the effect of epitaxial strain on the structural and magnetic properties of $CoFe_2O_4$ and $NiFe_2O_4$, i.e., with the elastic and magnetoelastic response of these systems. Here, we therefore give a brief overview over the general magnetoelastic theory for a cubic crystal, and present the most important equations that are used in Sec. III to analyze the results of our first-principles calculations.

The magnetoelastic energy density $f=E/V$ of a cubic crystal can be written as[31]

$$f=f_K+f_{\mathrm{el}}+f_{\mathrm{mel}}, \tag{1}$$

where the three individual terms describe the cubic (unstrained) magnetic anisotropy energy density f_K, the purely elastic energy density f_{el}, and the coupled magnetoelastic contribution f_{mel}, respectively. To lowest order in the strain tensor ε_{ij} and in the direction cosines α_i of the magnetization vector, these terms have the following forms:

$$f_K=K(\alpha_1^2\alpha_2^2+\alpha_2^2\alpha_3^2+\alpha_3^2\alpha_1^2), \tag{2}$$

$$\begin{aligned}f_{\mathrm{el}}=&\frac{1}{2}C_{11}(\varepsilon_{xx}^2+\varepsilon_{yy}^2+\varepsilon_{zz}^2)+\frac{1}{2}C_{44}(\varepsilon_{xy}^2+\varepsilon_{yz}^2+\varepsilon_{zx}^2)\\&+C_{12}(\varepsilon_{yy}\varepsilon_{zz}+\varepsilon_{xx}\varepsilon_{zz}+\varepsilon_{xx}\varepsilon_{yy}),\end{aligned} \tag{3}$$

$$\begin{aligned}f_{\mathrm{mel}}=&B_1(\alpha_1^2\varepsilon_{xx}+\alpha_2^2\varepsilon_{yy}+\alpha_3^2\varepsilon_{zz})\\&+B_2(\alpha_1\alpha_2\varepsilon_{xy}+\alpha_2\alpha_3\varepsilon_{yz}+\alpha_3\alpha_1\varepsilon_{zx}).\end{aligned} \tag{4}$$

Here, K denotes the lowest-order cubic anisotropy constant, C_{11}, C_{12}, and C_{44} are the elastic moduli, and B_1 and B_2 are magnetoelastic coupling constants.

The bulk modulus B is defined as

$$B=V_0\left(\frac{\partial^2E_{\mathrm{tot}}}{\partial V^2}\right)\Bigg|_{(V=V_0)}, \tag{5}$$

where E_{tot} is the total energy and V_0 is the equilibrium bulk volume. Using Eqs. (1)–(4), the bulk modulus of a cubic crystal can be expressed in terms of the elastic moduli C_{11} and C_{12},

$$B=\frac{1}{3}(C_{11}+2C_{12}). \tag{6}$$

In this work, we investigate the effect of epitaxial strain that is induced in thin-film samples by the lattice mismatch to the substrate. This situation can be described by a fixed in-plane strain $\varepsilon_{xx}=\varepsilon_{yy}=(a-a_0)/a_0$, where a is the in-plane lattice constant of the thin-film material and a_0 is the corresponding lattice constant in the bulk. The resulting out-of-plane strain $\varepsilon_{zz}=(c-a_0)/a_0$ can be obtained from Eqs. (1)–(4) together with the condition of vanishing stress for the out-of-plane lattice constant c, i.e., $\frac{\partial f}{\partial \varepsilon_{zz}}=0$. In the demagnetized state, ε_{zz} is related to the applied in-plane strain via the so-called two-dimensional (2D) Poisson ratio $\nu_{2\mathrm{D}}$,[32]

$$\nu_{2\mathrm{D}}=-\frac{\varepsilon_{zz}}{\varepsilon_{xx}}=2\frac{C_{12}}{C_{11}}. \tag{7}$$

After calculating both $\nu_{2\mathrm{D}}$ and the bulk modulus using DFT, the elastic moduli C_{11} and C_{12} can thus be obtained from Eqs. (6) and (7).

In Sec. III C, we monitor the differences in total energy for different orientations of the magnetization as a function of the in-plane constraint ε_{xx}. Using expression (7) for $\nu_{2\mathrm{D}}$ and taking the energy for orientation of the magnetization along the [001] direction as reference, i.e., $\Delta f_{hkl}=f_{001}-f_{hkl}$, one obtains

$$\begin{aligned}\Delta f_{\langle 100\rangle}&=-B_1(\nu_{2\mathrm{D}}+1)\epsilon_{xx},\\ \Delta f_{\langle 110\rangle}&=-B_1(\nu_{2\mathrm{D}}+1)\epsilon_{xx}-\frac{1}{4}K,\\ \Delta f_{\langle 111\rangle}&=-\frac{2}{3}B_1(\nu_{2\mathrm{D}}+1)\epsilon_{xx}-\frac{3}{4}K,\\ \Delta f_{\langle 101\rangle}&=-\frac{1}{2}B_1(\nu_{2\mathrm{D}}+1)\epsilon_{xx}-\frac{1}{4}K.\end{aligned} \tag{8}$$

Thus, the epitaxial strain dependence of these energy differences is governed by the magnetoelastic coupling constant B_1 and the two-dimensional Poisson ratio $\nu_{2\mathrm{D}}$.

Since the constant B_1 is not directly accessible by experiment, the linear magnetoelastic response is typically characterized by the magnetostriction constant λ_{100}, which is related to B_1 and the elastic moduli C_{11} and C_{12},

$$\lambda_{100}=-\frac{2}{3}\frac{B_1}{C_{11}-C_{12}}. \tag{9}$$

λ_{100} characterizes the relative change in length (lattice constant) along [100] when the material is magnetized along this direction, compared to the unmagnetized state.

C. Structural relaxations for the inverse spinel structure

As described in Sec. II A, the distribution of divalent and trivalent cations on the octahedrally coordinated B sites in the inverse spinel structure is assumed to be random for both $CoFe_2O_4$ and $NiFe_2O_4$. On the other hand, the periodic boundary conditions employed in our calculations always correspond to a specific cation arrangement with perfect long-range order. Even though a "quasirandom" distribution of divalent and trivalent cations could, in principle, be achieved by using a very large unit cell, the required computational effort would be prohibitively large. For simplicity, we therefore restrict ourselves to the smallest possible unit cell which contains two spinel formula units, i.e., four B sites. Distributing two Fe atoms on two of these sites, and filling the other two sites with either Co or Ni, lowers the symmetry from space group $Fd\bar{3}m$ (No. 227) to *Imma* (No. 74) independent of which of the four B sites are occupied by Fe [see Fig. 1(b)]. Different choices (settings) simply lead to different orientations of the orthorhombic axes relative to the Cartesian directions. It will become clear from the results presented in Sec. III that the specific cation arrangement used in our calculations does not critically affect our conclusions.

Within the lower *Imma* symmetry (and setting 1, see below), the tetrahedrally coordinated A sites are located on Wyckoff position 4e $(0,\frac{1}{4},z)$ whereas the octahedrally coordinated B sites split into Wyckoff positions 4b $(0,0,\frac{1}{2})$ and 4d $(\frac{1}{4},\frac{1}{4},\frac{3}{4})$. In addition, the oxygen positions split into Wyckoff positions 8i $(x,\frac{1}{4},z)$ and 8h $(0,y,z)$.

In order to minimize the effect of this artificial symmetry lowering, and to obtain results that are as close as possible to

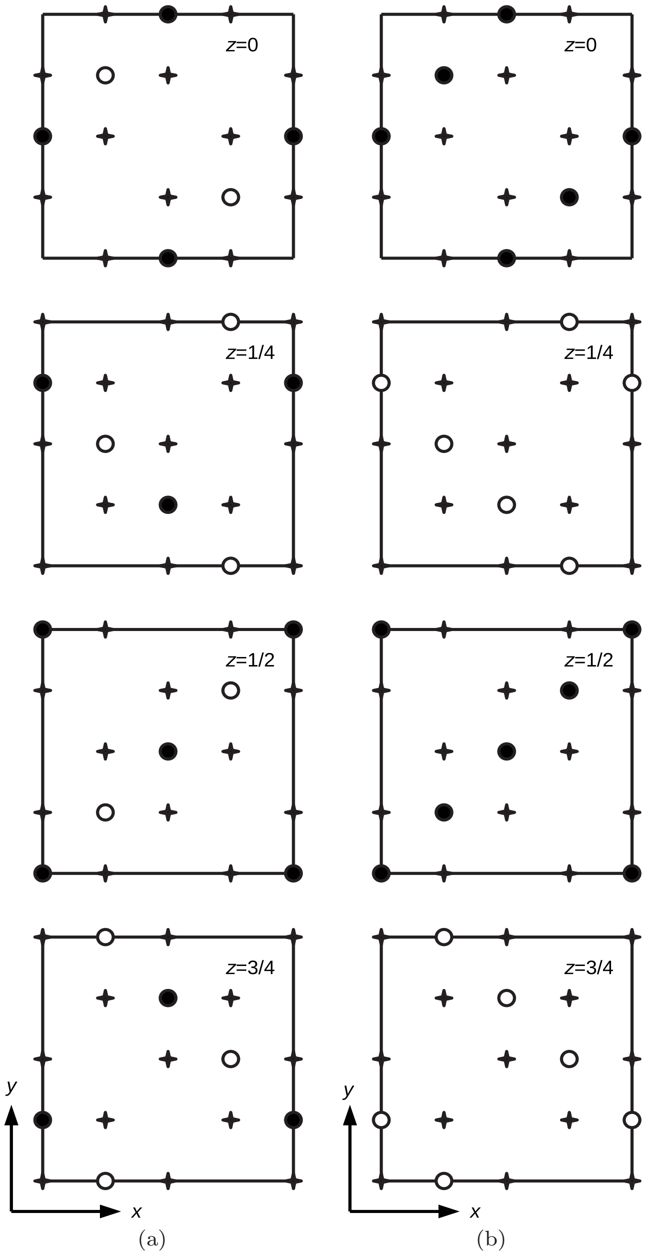

(a) (b)

FIG. 2. Cation distribution within different *x*-*y* planes for different values of *z*, corresponding to setting 1 (a) and setting 3 (b) (see main text for details). Only layers containing *B*-site cations are shown. Divalent cations (Co^{2+},Ni^{2+}) are depicted as filled black circles, trivalent cations (Fe^{3+}) as open black circles, and oxygen anions as black crosses. Note that we use the convention where the origin is located at the midpoint between two *A* sites.

the average cubic bulk symmetry seen in experiments, we apply the following constraints during our structural relaxations. For the calculations corresponding to the unstrained bulk case, we constrain the lattice parameters along the three Cartesian direction to be equal, $a=b=c$, and we fix the *A*-site cations to their ideal cubic positions, corresponding to $z(4\mathrm{e})=\frac{1}{8}$. On the other hand, since the oxygen positions are characterized by one free structural parameter already within cubic $Fd\bar{3}m$ symmetry [Wyckoff position 32e (u,u,u)], we do not apply any constraints to the 8i and 8h positions within *Imma* symmetry. The relaxed bulk structure is then found by relaxing all internal positions for different volumes and finding the volume that minimizes the total energy. For the relaxations corresponding to a certain value of epitaxial strain, we constrain the two in-plane lattice constants to be equal, and then vary the out-of-plane lattice constant *c* while relaxing all internal coordinates [except for $z(4\mathrm{e})=\frac{1}{8}$].

While for the unstrained bulk structure all possible *B*-site cation distributions that can be accommodated within the primitive fcc unit cell of the spinel structure lead to the same *Imma* symmetry, different cases can be distinguished once an epitaxial constraint is applied to the resulting structure. To illustrate this, the cation distributions for two different settings are depicted in Figs. 2(a) and 2(b). The *B*-site cation distribution (and the oxygen positions) within different *x*-*y* planes are shown, corresponding to different "heights" *z*. The different settings simply correspond to different orientations of the orthorhombic *Imma* crystal axes relative to the original cubic axes.

It can be seen from Fig. 2 that the *B* sites are arranged in an interconnected network of chains along ⟨110⟩-type directions. In setting 1 [Fig. 2(a)], the corresponding chains within the same *x*-*y* plane contain alternating divalent and trivalent cations. In contrast, for setting 3 [Fig. 2(b)] each *x*-*y* plane contains only one unique cation species, which then alternates between adjacent planes along the *z* direction [see also Fig. 1(b)]. In setting 1 the same alternating planes are oriented perpendicular to the *x* direction, whereas for setting 2 (not shown) these planes are oriented perpendicular to the *y* direction. If an epitaxial constraint is applied within the *x*-*y* plane, setting 3 becomes different from settings 1 and 2, with the difference being the orientation of the "substrate plane" relative to the planes defined by the cation order.

In view of this, we have performed all calculations corresponding to epitaxially strained systems for both setting 1 and setting 3. The differences between the results obtained for the two different settings then represent a measure for the sensitivity of these results from the specific cation arrangement used in our calculations.

D. Other computational details

All calculations presented in this work were performed using the projector-augmented wave (PAW) method,[33] implemented in the Vienna *ab initio* simulation package (VASP 4.6).[34–37] Standard PAW potentials supplied with VASP were used in the calculations, contributing nine valence electrons per Co($4s^2 3d^7$), 16 valence electrons per Ni($3p^6 4s^2 3d^8$), 14 valence electrons per Fe($3p^6 4s^2 3d^6$), and 6 valence electrons per O($2s^2 2p^4$). A plane wave energy cutoff of 500 eV was used, and the Brillouin zone was sampled using different *k*-point grids centered at the Γ point. A $5\times5\times5$ *k*-point grid was used for the structural optimization and all total-energy calculations whereas a finer $7\times7\times7$ grid was used to calculate densities of states (DOSs). The tetrahedron method with Blöchl corrections was used for Brillouin-zone integration.[33] We have verified that all quantities of interest, in particular, the MAEs, are well converged for the used *k*-point grid and energy cutoff. All structural relaxations were

TABLE I. Optimized bulk lattice constants a_0 and bulk moduli B for $CoFe_2O_4$ and $NiFe_2O_4$, calculated using the LSDA+U, GGA, and GGA+U exchange-correlation functionals in comparison with experimental data.

	$CoFe_2O_4$		$NiFe_2O_4$	
	a_0 (Å)	B (GPa)	a_0 (Å)	B (GPa)
LSDA+U	8.231	206.0	8.196	213.1
GGA	8.366	211.0	8.346	166.2
GGA+U	8.463	172.3	8.426	177.1
Expt. (Ref. 42)	8.392	185.7	8.339	198.2
Expt. (Ref. 43)	8.35		8.325	

performed within a scalar-relativistic approximation whereas spin-orbit coupling was included in the calculation of the MAEs.

As already noted in Sec. II A, $CoFe_2O_4$ and $NiFe_2O_4$ are small gap insulators, whereas half metallic or, in the case of $NiFe_2O_4$, only marginally insulating band structures have been obtained in previous LSDA calculations.[24] In the present work we therefore use the LSDA+U and GGA+U approach,[38] which is known to give a good description of the electronic structure for many transition-metal oxides.[39] We employ the Hubbard "+U" correction in the simplified, rotationally invariant version of Dudarev *et al.*,[40] where the same value $U_{\mathrm{eff}}=U-J=3$ eV is used for all transition metal cations. The corresponding results are compared to pure GGA calculations, using the GGA approach of Perdew, Burke, and Ernzerhof.[41] [We restricted the comparison to pure GGA since Perron *et al.*[28] presented some evidence (for $NiFe_2O_4$) that LSDA might not be appropriate to properly describe these materials.]

Values for the local magnetic moments and atom-projected DOS are obtained by integration of the appropriate quantities over atom-centered spheres with radii taken from the applied PAW potentials [1.164 Å (Fe), 1.302 Å (Co), and 1.058 Å (Ni)], respectively.

III. RESULTS AND DISCUSSION

A. Unstrained bulk structures

We first present our results for the unstrained bulk structures. The calculated lattice constants and bulk moduli for both $CoFe_2O_4$ and $NiFe_2O_4$ using different exchange-correlation functionals are summarized in Table I. It can be seen that for both $CoFe_2O_4$ and $NiFe_2O_4$ the use of LSDA +U leads to an underestimation of the lattice constant by $\sim 2\%$ and an overestimation of the bulk modulus by $\sim 10\%$ compared to the experimental values. The opposite trend is observed for GGA+U (overestimation of lattice constant by $\sim 1\%$ and underestimation of bulk modulus by $\sim 10\%$). These deviations from the experimental values are typical for complex transition-metal oxides (see, e.g., Refs. 44–46). The differences between LSDA+U and GGA+U result from the differences in the underlying DFT exchange-correlation functional (LSDA versus GGA), which typically lead to differences in lattice constant and bulk moduli that are of similar magnitude than the difference between our LSDA+U and GGA+U results (see, e.g., Ref. 47).

Interestingly, the lattice constants calculated within pure GGA match the experimental values almost perfectly for both $CoFe_2O_4$ and $NiFe_2O_4$. However, this is somewhat fortuitous and probably due to a cancellation of errors, as can be seen by the large discrepancies in the bulk moduli. It will become clear in the following, that the +U correction is necessary in order to obtain a good description of the electronic structure for both $CoFe_2O_4$ and $NiFe_2O_4$.

TABLE II. Calculated Wyckoff parameters (setting 1) for the oxygen anions 8h $(x,\frac{1}{4},z)$ and 8i $(0,y,z)$ for $CoFe_2O_4$ and $NiFe_2O_4$ using different exchange-correlation functionals. The last line lists the corresponding parameters resulting from Wyckoff position 32e (u,u,u) within $Fd\bar{3}m$ symmetry, $\bar{u}$ is obtained from these relations by averaging over recalculated u values for each data set.

	8i		8h		
$CoFe_2O_4$	x	z	y	z	$\bar{u}$
LSDA+U	0.235	−0.498	0.009	−0.257	0.255
GGA	0.240	−0.496	0.008	−0.255	0.255
GGA+U	0.234	−0.499	0.007	−0.259	0.255
	8i		8h		
$NiFe_2O_4$	x	z	y	z	$\bar{u}$
LSDA+U	0.237	−0.495	0.010	−0.258	0.256
GGA	0.239	−0.496	0.009	−0.257	0.255
GGA+U	0.235	−0.496	0.008	−0.258	0.256
$Fd\bar{3}m$	$\frac{3}{4}-2u$	$u-\frac{3}{4}$	$2u-\frac{1}{2}$	$-u$	

As discussed in Sec. II C, the cation arrangement in our unit cell lowers the symmetry to orthorhombic *Imma*, with four independent parameters describing the positions of the oxygen anions at Wyckoff positions 8h and 8i, compared to one parameter for Wyckoff position 32e in the cubic space group $Fd\bar{3}m$. Table II lists the corresponding Wyckoff parameters obtained from our structural optimizations. It can be seen that differences between different exchange-correlation functionals are rather small.

The last line in Table II indicates the relation between the Wyckoff positions 8i and 8h in the *Imma* space group (setting 1) and Wyckoff position 32e (u,u,u) in cubic $Fd\bar{3}m$ symmetry (assuming that no actual symmetry breaking occurs). These relations allow us to obtain an average Wyckoff parameter $\bar{u}$, by calculating the value of u corresponding to each of the four calculated Wyckoff parameters x(8i), z(8i), y(8h), and z(8h) for each data set and subsequent averaging. The resulting values for $\bar{u}$ agree very well with available experimental data, which are 0.256 for $CoFe_2O_4$ and 0.257 for $NiFe_2O_4$.[43] Furthermore, the values calculated from the individual 8h and 8i Wyckoff parameters deviate only very little from the average values, which indicates that the lower symmetry used in our calculation has only a negligible effect on the internal structural parameters.

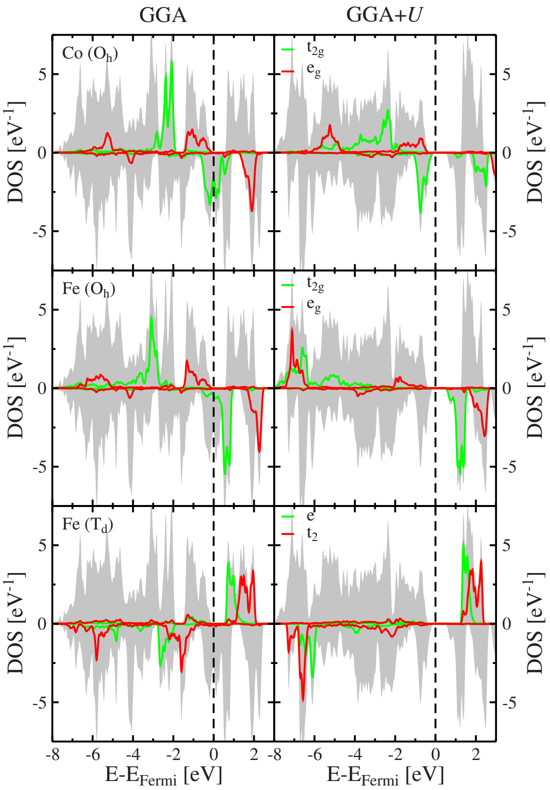

FIG. 3. (Color online) Total and projected DOS per formula unit for $CoFe_2O_4$. Left (right) panels correspond to GGA (GGA+U) calculations. The d states of Co(O_h) (upper panels), Fe(O_h) (middle panels), and Fe(T_d) (lower panels) are separated into t_{2g} (green/dark gray) and e_g (red/black) contributions for the O_h sites and into e (green/dark gray) and t_2 (red/black) contributions for the T_d sites. The total DOS is shown as shaded gray area in all panels. Majority-(minority-) spin projections correspond to positive (negative) values.

Figures 3 and 4 show the calculated spin-decomposed DOSs for $CoFe_2O_4$ and $NiFe_2O_4$, respectively, within the optimized bulk structure and using both pure GGA and GGA+U. Both the total DOS per formula unit and the projected DOS per ion for the d states of the various transition metal cations are shown, the latter separated into t_{2g}/e_g and e/t_2 contributions, respectively. The DOS calculated within LSDA+U (not shown) do not show any significant differences compared to the ones calculated using GGA+U.

From the projected DOS, it can be seen that all transition-metal cations are in high-spin states, with one spin projection completely occupied, and that the cubic component of the crystal field on the octahedrally coordinated (O_h) sites lowers the t_{2g} states relative to the e_g states whereas on the tetrahedrally coordinated (T_d) sites the e states are slightly lower in energy than the t_2 states. Due to the Néel-type ferrimagnetic order, the local majority-spin direction on the T_d sites is reversed relative to the O_h sites.

It is apparent that within GGA $CoFe_2O_4$ turns out to be a half metal, in contrast to the insulating behavior found in experiment.[23] This is similar to what has been found in previous LSDA calculations.[24] The half metallicity is due to the partial filling of the minority t_{2g} states of Co(O_h), which in

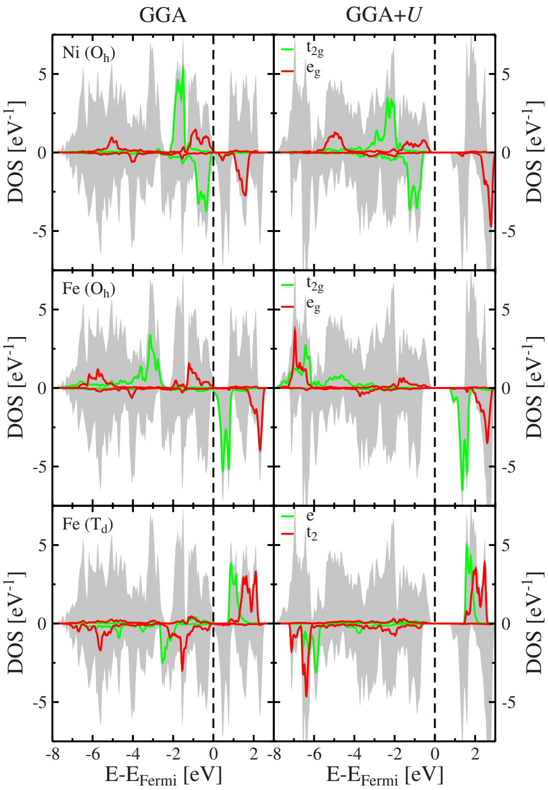

FIG. 4. (Color online) Total and projected DOS per formula unit for $NiFe_2O_4$. Left (right) panels correspond to GGA (GGA+U) calculations. The d states of Ni(O_h) (upper panels), Fe(O_h) (middle panels), and Fe(T_d) (lower panels) are separated into t_{2g} (green/dark gray) and e_g (red/black) contributions for the O_h sites and into e (green/dark gray) and t_2 (red/black) contributions for the T_d sites. The total DOS is shown as shaded gray area in all panels. Majority-(minority-) spin projections correspond to positive (negative) values.

turn results from the formal d^7 configuration of the Co^{2+} cation (see upper left panel of Fig. 3). This apparent deficiency of the GGA approach is corrected within the GGA $+U$ calculation as can be seen in the right part of Fig. 3. We note that this is very similar to the case of rocksalt CoO, which also contains Co^{2+} with a d^7 electron configuration that leads to a metallic solution in pure LSDA (Ref. 48) whereas application of the DFT$+U$ approach leads to an insulating state in agreement with the experimental observations.[38]

The Hubbard correction splits the occupied and unoccupied parts of the minority spin t_{2g} states of the Co^{2+} cations (see upper right panel of Fig. 3), thereby opening an energy gap. In addition, the local spin splitting on the Fe cation is drastically enhanced, shifting the local majority-spin d states toward the bottom of the valence band. We note that once the value of U_{eff} on the Co sites is large enough to push the corresponding unoccupied minority-spin t_{2g} states above the lowest minority-spin Fe(O_h) states, the width of the band gap is determined by the difference in energy between these lowest unoccupied minority-spin Fe states and the highest occupied minority spin t_{2g} states of Co(O_h). Therefore, a further increase in U_{eff} on the Co sites does not significantly change the size of the band gap. Similarly, the band gap depends only weakly on the specific value of U_{eff} on the Fe sites.

The gap size of 0.9 eV obtained within GGA$+U$ for the chosen values of U_{eff} is comparable to the 0.63 eV obtained by Antonov *et al.* using LSDA$+U$ with $U_{\text{eff}}=4.0$ eV for the Co(O_h) and $U_{\text{eff}}=4.5$ eV for the Fe(O_h) and Fe(T_d) cations,[25] and also agrees well with the value of 0.8 eV reported by Szotek *et al.* utilizing a self-interaction corrected LSDA approach.[26]

Ni^{2+} formally has one additional electron compared to Co^{2+}, leading to a fully occupied minority-spin t_{2g} manifold for the Ni^{2+} cation within a cubic (O_h) crystal field. Accordingly, $NiFe_2O_4$ exhibits a tiny gap of ~0.1 eV between the occupied minority-spin t_{2g} states of Ni(O_h) and the unoccupied minority t_{2g} states of Fe(O_h) even in pure GGA (see left panels of Fig. 4). However, the use of GGA$+U$ leads to a significant enlargement of this energy gap to a more realistic value of 0.97 eV for the chosen values of U_{eff}. This is in good agreement with band gaps of 0.99 and 0.98 eV reported by Antonov *et al.*[25] and Szotek *et al.*,[26] respectively. Similar to the case of $CoFe_2O_4$, the Hubbard correction also leads to a strong enhancement of the local spin splitting on the Fe sites in $NiFe_2O_4$.

Table III shows the local magnetic moments of the transition-metal cations per formula unit calculated within the three different approaches. The total magnetic moment is independent of the applied exchange-correlation functional, and equal to the integer value that follows from the formal electron configuration of the transition-metal cations and the Néel-type ferrimagnetic arrangement (3 μ_B for $CoFe_2O_4$ and 2 μ_B for $NiFe_2O_4$). This is a result of the either half-metallic or insulating character of the underlying electronic structures. Nevertheless, as can be seen in Table III, the Hubbard correction has a significant influence on the spatial distribution of the magnetization density and the use of GGA $+U$ (and LSDA$+U$) leads to more localized magnetic moments compared to GGA, indicated by the increased magnetic moments corresponding to the different cation sites.

TABLE III. Calculated magnetic moments (in μ_B) for bulk $CoFe_2O_4$ and $NiFe_2O_4$ using different exchange-correlation functionals. The total magnetic moment per formula unit amounts to 3 μ_B (2 μ_B) for $CoFe_2O_4$ ($NiFe_2O_4$), respectively.

$CoFe_2O_4$	Co(O_h)	Fe(O_h)	Fe(T_d)
LSDA$+U$	+2.52	+3.99	−3.82
GGA	+2.43	+3.66	−3.45
GGA$+U$	+2.62	+4.10	−3.98
$NiFe_2O_4$	Ni(O_h)	Fe(O_h)	Fe(T_d)
LSDA$+U$	+1.49	+4.00	−3.82
GGA	+1.36	+3.71	−3.46
GGA$+U$	+1.58	+4.11	−3.97

The results presented in this section indicate that for a realistic and consistent description of the structural, electronic, and magnetic properties of both $CoFe_2O_4$ and $NiFe_2O_4$, a Hubbard correction to either LSDA or GGA is required. In the following, we will therefore present only results obtained within the LSDA$+U$ and GGA$+U$ approaches.

B. Epitaxial strain and elastic properties

Figure 5 shows the relaxed c/a ratio of $NiFe_2O_4$ as function of the epitaxial constraint ε_{xx}, obtained from GGA$+U$ calculations as described in Sec. II C. The case of $CoFe_2O_4$ is very similar. Two important things can be seen from this. First, due to the orthorhombic *Imma* symmetry of the chosen cation arrangement on the O_h sites, the c/a ratio is not exactly equal to 1 at zero strain. However, this effect is clearly negligible compared to the changes in c/a induced by epitaxial strains of order ~1% and therefore does not affect our further analysis. Second, the slope of the c/a ratio, which characterizes the elastic response of the material, is nearly completely unaffected by the different cation arrangements. These results provide evidence that the unit cell and cation

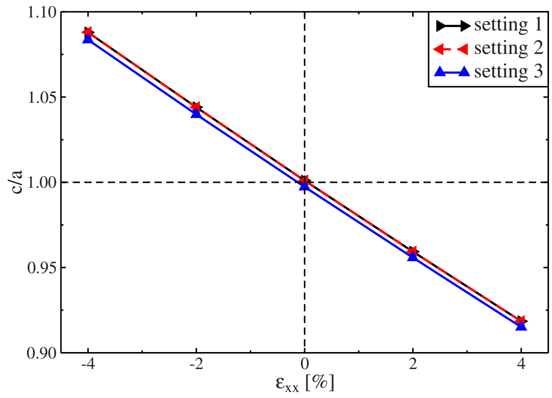

FIG. 5. (Color online) Calculated c/a ratio of $NiFe_2O_4$ as a function of epitaxial strain ε_{xx} obtained from GGA$+U$ calculations and different cation arrangements (settings) on the O_h sites.

TABLE IV. Bulk modulus B, two-dimensional Poisson ratio ν_{2D}, and elastic coefficients C_{11} and C_{12} for $CoFe_2O_4$ and $NiFe_2O_4$, obtained for different exchange-correlation potentials and different cation arrangements (setting s), in comparison to experimental data. The experimental ν_{2D} has been evaluated from Eq. (7) using the experimental elastic constants.

$CoFe_2O_4$	s	B (GPa)	ν_{2D}	C_{11} (GPa)	C_{12} (GPa)
LSDA+U	1	206.0	1.191	282.0	167.9
	3		1.185	282.7	167.6
GGA+U	1	172.3	1.147	240.8	138.1
	3		1.132	242.5	137.3
Expt. (Ref. 42)		185.7	1.167	257.1	150.0
$NiFe_2O_4$	S	B (GPa)	ν_{2D}	C_{11} (GPa)	C_{12} (GPa)
LSDA+U	1	213.1	1.172	294.4	172.5
	3		1.167	295.1	172.2
GGA+U	1	177.1	1.115	251.2	140.0
	3		1.106	252.2	139.5
Expt. (Ref. 42)		198.2	1.177	273.1	160.7

arrangement used in the present work is sufficient to obtain accurate structural and elastic properties that are representative for the inverse spinel structure with randomly distributed cations on the O_h sites.

From the data shown in Fig. 5, we can therefore obtain the two-dimensional Poisson ratio ν_{2D} [Eq. (7)], which relates in-plane and out-of-plane strains. Together with the bulk moduli listed in Table I, we can then determine the two elastic constants C_{11} and C_{12} from Eqs. (6) and (7).

The calculated two-dimensional Poisson ratios ν_{2D} and elastic constants C_{11} and C_{12}, together with the bulk moduli already presented in Table I, are listed in Table IV, and are compared with experimental results from Ref. 42. It can be seen that, as already pointed out, the specific cation arrangement has nearly no influence on the value of ν_{2D} and thus C_{11} and C_{12}. On the other hand, the specific choice of either LSDA+U or GGA+U has a noticeable effect. Similar to the case of the bulk modulus, we observe an overestimation (underestimation) of the elastic constants C_{11} and C_{12} in the LSDA+U (GGA+U) calculations. The same general trend holds for the two-dimensional Poisson ratio of $CoFe_2O_4$ while for $NiFe_2O_4$ the use of LSDA+U also slightly underestimates ν_{2D}. Overall the deviations are only within a few percent of the experimental data (1–2 % for $CoFe_2O_4$ and up to 6% for $NiFe_2O_4$), and we therefore conclude that both LSDA+U and GGA+U allow for a good description of the strain response of $CoFe_2O_4$ and $NiFe_2O_4$.

C. Magnetoelastic coupling

The calculated MAEs, defined as the energy differences for various orientations of the magnetization relative to the energy for orientation of the magnetization parallel to the [001] direction, are depicted in Fig. 6 for $CoFe_2O_4$ (GGA+U only) and in Fig. 7 for $NiFe_2O_4$ (both LSDA+U and GGA+U). It can be seen that the calculated MAEs for $CoFe_2O_4$ are roughly five to six times larger than in $NiFe_2O_4$. Furthermore, to a good approximation, the calculated energy differences exhibit a linear dependence on strain. Deviations from this linear behavior are most pronounced for the case of $NiFe_2O_4$ within setting 3. Since the pure elastic response shown in Fig. 5 does not exhibit any significant nonlinearities, we conclude that higher-order magnetoelastic terms are responsible for the slightly nonlinear behavior of the MAE in this case.

It can also be seen, that in all cases the strain dependence, i.e., the slope of the various curves shown in Figs. 6 and 7, is largest for the in-plane versus out-of-plane energy differences, i.e., for orientation of the magnetization along the [100], [010], [110], and [1$\bar{1}$0] directions (compared to the [001] direction), consistent with Eqs. (8). Thus, tensile strain

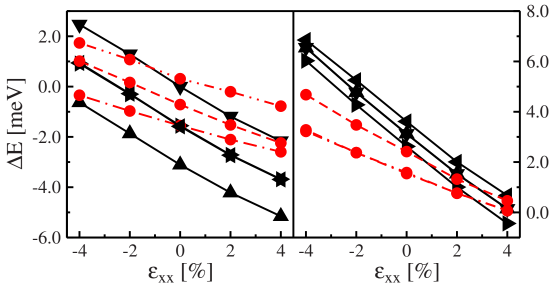

FIG. 6. (Color online) $CoFe_2O_4$ GGA+U total-energy differences for orientation of the magnetization along various crystallographic in-plane directions with respect to the [001] direction (black solid lines): ▲ [100], ▼ [010], ◀ [110], and ▶ [1$\bar{1}$0]. Red broken lines denote crystallographic directions which include also out-of-plane components, namely, [101] (dashed-dotted line), [011] (dashed-double dotted line), and [111] (dashed line). Left (right) panels contain the results corresponding to setting 1 (setting 3).

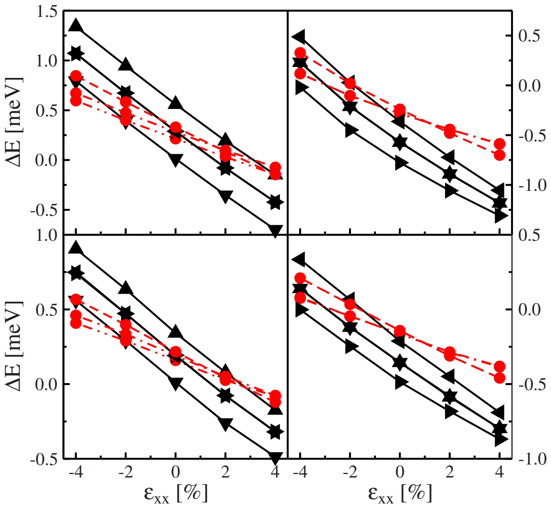

FIG. 7. (Color online) $NiFe_2O_4$ LSDA+U (GGA+U) total-energy differences for orientation of the magnetization along various crystallographic in-plane directions with respect to the [001] direction are shown in the upper (lower) panels (black solid lines): ▲ [100], ▼ [010], ◀ [110], and ▶ [$1\bar{1}0$]. Red broken lines denote crystallographic directions which include also out-of-plane components, namely, [101] (dashed-dotted line), [011] (dashed-double dotted line), and [111] (dashed line). Left (right) panels contain the results corresponding to setting 1 (setting 3).

favors perpendicular anisotropy (easy axis perpendicular to the "substrate") and compressive strain favors in-plane orientation of the magnetization, i.e., $B_1 > 0$. For sufficient amount of strain the easy axis of magnetization will therefore always be oriented either in-plane or out-of-plane, consistent with various experimental observations in thin $CoFe_2O_4$ films under tensile strain.[13,14,49]

According to the phenomenological magnetoelastic theory for a cubic crystal discussed in Sec. II B, in particular, Eq. (8), the strain dependence of the in-plane versus out-of-plane anisotropy should be stronger by a factor of 2 compared to the anisotropy corresponding to [101] or [011] orientation of the magnetization, and by a factor of 3/2 compared to [111] orientation. We note that these ratios are very well observed by the calculated anisotropy energies shown in Figs. 6 and 7. This indicates that the strain dependence of the calculated anisotropy energies is rather independent of the specific cation arrangement, which allows us to obtain the magnetoelastic constants of $CoFe_2O_4$ and $NiFe_2O_4$ from our calculations.

On the other hand, we recall that due to the specific cation arrangement used in the calculations, and the resulting symmetry lowering from cubic to orthorhombic, the three cubic axes are not equivalent even for zero strain. For setting 1 the y and z directions are equivalent, but different from x, whereas for setting 3 x and y are equivalent but different from z. This is reflected in the calculated anisotropy energies for zero strain (ε_{xx}=0), which in setting 1 are largest between z/y and the x direction. (Note that for zero strain both settings are completely equivalent apart from a rotation of the coordinate axes by 120° around the [111] direction.) The anisotropy induced by the symmetry lowering to orthorhombic is therefore at least of the same magnitude as the cubic anisotropy in the disordered inverse spinel structure, and the calculated anisotropy energies for zero strain are therefore not representative for the inverse spinel structure with random distribution of cations on the O_h sites, i.e., the cubic anisotropy constant K cannot be determined from our calculations.

From the data shown in Figs. 6 and 7, we thus obtain the magnetoelastic coefficients B_1 by using the appropriate equation out of Eq. (8) (together with the calculated values for ν_{2D}) for each calculated energy difference individually, and then average over the resulting values for B_1 within the same setting and for the same exchange-correlation functional. From the so-obtained magnetoelastic coefficients B_1, we then calculate the linear magnetostriction coefficient λ_{100} from Eq. (9) using the elastic moduli determined in Sec. III B. The resulting values for both B_1 and λ_{100} are listed in Table V.

It can be seen that overall the calculated magnetostriction constants are in very good agreement with available experimental data, despite the difficulties related to the specific choice of cation arrangement and exchange-correlation functional. In particular, the large difference in magnetostriction between $CoFe_2O_4$ and $NiFe_2O_4$ is well reproduced by the calculations. For $NiFe_2O_4$, the difference in the calculated values for λ_{100} due to the use of either LSDA+U and GGA+U is larger than the effect of the different cation settings. For $CoFe_2O_4$, the cation arrangement seems to have a larger influence on λ_{100} than for $NiFe_2O_4$. This is consistent with the large spread in the experimentally obtained magnetostriction for $CoFe_2O_4$, where different preparation conditions can lead to differences in cation distribution/inversion or slightly off-stoichiometric compositions. In addition, only very few measurements have been performed on single crystals whereas only a superposition of λ_{100} and λ_{111} can be measured for polycrystalline samples.

The rather good agreement between our calculated values for λ_{100} and the available experimental data demonstrates that, in principle, a quantitative calculation of magnetostriction in spinel ferrites is feasible, in spite of the difficulties related to the inverse spinel structure with random cation distribution on the B site, and the usual difficulties regarding an accurate description of exchange and correlation effects in transition-metal oxides.

IV. SUMMARY AND OUTLOOK

In summary, we have presented a systematic first-principles study of the effect of epitaxial strain on the structural and magnetostructural properties of $CoFe_2O_4$ and $NiFe_2O_4$ spinel ferrites. Special care was taken to assess the quantitative uncertainties resulting from different treatments of exchange-correlation effects and different cation arrangements used to represent the inverse spinel structure.

It has been shown, in agreement with earlier works, that "beyond LSDA/GGA" methods are required for a proper description of the electronic and magnetic properties of spinel ferrites $CoFe_2O_4$ and $NiFe_2O_4$. The +U approach used in the present work leads to a realistic electronic structure and good quantitative agreement with available experimental data for

TABLE V. Magnetoelastic coupling constant B_1 and magnetostriction constant λ_{100} for $CoFe_2O_4$ and $NiFe_2O_4$ using different exchange-correlation functionals and cation arrangements (setting s) in comparison with available experimental data.

		$CoFe_2O_4$		$NiFe_2O_4$	
	s	B_1 (MPa)	λ_{100} ($\times 10^{-6}$)	B_1 (MPa)	λ_{100} ($\times 10^{-6}$)
LSDA+U	1			10.03	−54.9
	3			9.65	−52.3
GGA+U	1	29.23	−189.7	6.72	−40.3
	3	39.74	−251.7	6.08	−35.9
Expt.			−225.0[a]		−50.9[b]
			−250.0[c]		−36.0[d]
			−590.0[e]		

[a] Polycrystalline $CoFe_2O_4$ (Ref. 50).
[b] Single crystals of $NiFe_2O_4$ (Ref. 52).
[c] Single crystals with $Co_{1.1}Fe_{1.9}O_4$ composition (Ref. 51).
[d] Single crystals with $Ni_{0.8}Fe_{2.2}O_4$ composition (Ref. 51).
[e] Single crystals with $Co_{0.8}Fe_{2.2}O_4$ composition (Ref. 51).

lattice, elastic, and magnetostrictive constants.

We find that the specific cation arrangement used to represent the inverse spinel structure has only little effect on the structural properties. The corresponding effect on the magnetoelastic constants is also weak, with a somewhat stronger influence in the case of $CoFe_2O_4$. The latter fact is consistent with the considerable spread in the reported values for the magnetostriction constant for different samples of this material. In general, the starting point for the +U correction, i.e. either LSDA or GGA, has a somewhat stronger influence on the calculated materials constants than the different cation settings.

However, in spite of these uncertainties, the overall agreement between our results and experimental data is very good. In particular, the calculated magnetostriction constants λ_{100} of about −45 ppm for $NiFe_2O_4$ and about −220 ppm for $CoFe_2O_4$ fall well into the spectra of available experimental values obtained from different samples (see Table V). Consistent with the negative sign of λ_{100}, the easy magnetization direction changes from in-plane for compressive epitaxial strain to out-of-plane for tensile strain. This gives further confirmation that the reorientation of the easy axis observed experimentally in thin films of $CoFe_2O_4$ under different conditions is indeed predominantly strain driven.[13,14,49]

In summary, our results indicate that a quantitative description of both structural and magnetoelastic properties in spinel ferrites is possible within the DFT+U approach, which opens the way for future computational studies of these materials. Such calculations can then provide important information regarding the effect of cation inversion and off-stoichiometry, which can be used to optimize magnetostriction constants and anisotropy in spinel ferrites.

ACKNOWLEDGMENTS

This work was supported by Science Foundation Ireland under Reference No. SFI-07/YI2/I1051 and made use of computational facilities provided by the Trinity Centre for High Performance Computing (TCHPC) and the Irish Centre for High-End Computing (ICHEC). D.F. acknowledges fruitful discussions with M. Richter and K. Koepernik.

---

*fritschd@tcd.ie

[1] V. A. M. Brabers, *Handbook of Magnetic Materials* (Elsevier, New York, 1995), Vol. 8, pp. 189–324.

[2] H. Zheng *et al.*, Science **303**, 661 (2004).

[3] F. Zavaliche *et al.*, Nano Lett. **5**, 1793 (2005).

[4] N. Dix, V. Skumryev, V. Laukhin, L. Fàbrega, F. Sánchez, and J. Fontcuberta, Mater. Sci. Eng., B **144**, 127 (2007).

[5] R. Muralidharan, N. Dix, V. Skumryev, M. Varela, F. Sánchez, and J. Fontcuberta, J. Appl. Phys. **103**, 07E301 (2008).

[6] U. Lüders *et al.*, J. Appl. Phys. **99**, 08K301 (2006).

[7] M. G. Chapline and S. X. Wang, Phys. Rev. B **74**, 014418 (2006).

[8] A. V. Ramos, T. S. Santos, G. X. Miao, M.-J. Guittet, J.-B. Moussy, and J. S. Moodera, Phys. Rev. B **78**, 180402 (2008).

[9] Y. Suzuki, Annu. Rev. Mater. Res. **31**, 265 (2001).

[10] U. Lüders, M. Bibes, J.-F. Bobo, M. Cantoni, R. Bertacco, and J. Fontcuberta, Phys. Rev. B **71**, 134419 (2005).

[11] S. Zhou *et al.*, Phys. Rev. B **80**, 094409 (2009).

[12] W. Huang, J. Zhu, H. Z. Zeng, X. H. Wei, Y. Zhang, and Y. R. Li, Appl. Phys. Lett. **89**, 262506 (2006).

[13] A. Lisfi, C. M. Williams, L. T. Nguyen, J. C. Lodder, A. Coleman, H. Corcoran, A. Johnson, P. Chang, A. Kumar, and W. Morgan, Phys. Rev. B **76**, 054405 (2007).

[14] X. S. Gao, D. H. Bao, B. Birajdar, T. Habisreuther, R. Mattheis,

M. A. Schubert, M. Alexe, and D. Hesse, J. Phys. D **42**, 175006 (2009).

[15] U. Lüders, A. Barthélémy, M. Bibes, K. Bouzehouane, S. Fusil, E. Jacquet, J.-P. Contour, J.-F. Bobo, J. Fontcuberta, and A. Fert, Adv. Mater. **18**, 1733 (2006).

[16] F. Rigato, S. Estradé, J. Arbiol, F. Peiró, U. Lüders, X. Martí, F. Sánchez, and J. Fontcuberta, Mater. Sci. Eng., B **144**, 43 (2007).

[17] P. Hohenberg and W. Kohn, Phys. Rev. **136**, B864 (1964).

[18] W. Kohn and L. J. Sham, Phys. Rev. **140**, A1133 (1965).

[19] R. O. Jones and O. Gunnarsson, Rev. Mod. Phys. **61**, 689 (1989).

[20] We note that a recent article by V. G. Ivanov, M. V. Abrashev, M. N. Iliev, M. M. Gospodinov, J. Meen, and M. I. Aroyo, Phys. Rev. B **82**, 024104 (2010), reports evidence for a short-range *B*-site order in $NiFe_2O_4$.

[21] L. Néel, Ann. Phys. (Paris) **3**, 137 (1948).

[22] R. D. Waldron, Phys. Rev. **99**, 1727 (1955).

[23] G. H. Jonker, J. Phys. Chem. Solids **9**, 165 (1959).

[24] M. Pénicaud, B. Siberchicot, C. B. Sommers, and J. Kübler, J. Magn. Magn. Mater. **103**, 212 (1992).

[25] V. N. Antonov, B. N. Harmon, and A. N. Yaresko, Phys. Rev. B **67**, 024417 (2003).

[26] Z. Szotek, W. M. Temmerman, D. Ködderitzsch, A. Svane, L. Petit, and H. Winter, Phys. Rev. B **74**, 174431 (2006).

[27] X. Zuo, S. Yan, B. Barbiellini, V. G. Harris, and C. Vittoria, J. Magn. Magn. Mater. **303**, e432 (2006).

[28] H. Perron, T. Mellier, C. Domain, J. Roques, E. Simoni, R. Drot, and H. Catalette, J. Phys.: Condens. Matter **19**, 346219 (2007).

[29] H.-T. Jeng and G. Y. Guo, J. Magn. Magn. Mater. **239**, 88 (2002).

[30] H.-T. Jeng and G. Y. Guo, J. Magn. Magn. Mater. **240**, 436 (2002).

[31] C. Kittel, Rev. Mod. Phys. **21**, 541 (1949).

[32] P. Harrison, *Quantum Wells, Wires and Dots: Theoretical and Computational Physics of Semiconductor Nanostructures*, 2nd ed. (Wiley-Interscience, Chichester, 2005).

[33] P. E. Blöchl, Phys. Rev. B **50**, 17953 (1994).

[34] G. Kresse and J. Hafner, Phys. Rev. B **47**, 558 (1993).

[35] G. Kresse and J. Hafner, Phys. Rev. B **49**, 14251 (1994).

[36] G. Kresse and J. Furthmüller, Comput. Mater. Sci. **6**, 15 (1996).

[37] G. Kresse and J. Furthmüller, Phys. Rev. B **54**, 11169 (1996).

[38] V. I. Anisimov, J. Zaanen, and O. K. Andersen, Phys. Rev. B **44**, 943 (1991).

[39] V. I. Anisimov, F. Aryasetiawan, and A. I. Liechtenstein, J. Phys.: Condens. Matter **9**, 767 (1997).

[40] S. L. Dudarev, G. A. Botton, S. Y. Savrasov, C. J. Humphreys, and A. P. Sutton, Phys. Rev. B **57**, 1505 (1998).

[41] J. P. Perdew, K. Burke, and M. Ernzerhof, Phys. Rev. Lett. **77**, 3865 (1996).

[42] Z. Li, E. S. Fisher, J. Z. Liu, and M. V. Nevitt, J. Mater. Sci. **26**, 2621 (1991).

[43] R. J. Hill, J. R. Craig, and G. V. Gibbs, Phys. Chem. Miner. **4**, 317 (1979).

[44] C. J. Fennie and K. M. Rabe, Phys. Rev. Lett. **96**, 205505 (2006).

[45] J. B. Neaton, C. Ederer, U. V. Waghmare, N. A. Spaldin, and K. M. Rabe, Phys. Rev. B **71**, 014113 (2005).

[46] C. Ederer and N. A. Spaldin, Curr. Opin. Solid State Mater. Sci. **9**, 128 (2005).

[47] G. I. Csonka, J. P. Perdew, A. Ruzsinszky, P. H. T. Philipsen, S. Lebègue, J. Paier, O. A. Vydrov, and J. G. Ángyán, Phys. Rev. B **79**, 155107 (2009).

[48] K. Terakura, T. Oguchi, A. R. Williams, and J. Kübler, Phys. Rev. B **30**, 4734 (1984).

[49] A. Lisfi, C. M. Williams, A. Johnson, L. T. Nguyen, J. C. Lodder, H. Corcoran, P. Chang, and W. Morgan, J. Phys.: Condens. Matter **17**, 1399 (2005).

[50] Y. Chen, J. E. Snyder, C. R. Schwichtenberg, K. W. Dennis, R. W. McCallum, and D. C. Jiles, IEEE Trans. Magn. **35**, 3652 (1999).

[51] R. M. Bozorth, E. F. Tilden, and A. J. Williams, Phys. Rev. **99**, 1788 (1955).

[52] A. B. Smith and R. V. Jones, J. Appl. Phys. **37**, 1001 (1966).